scientific reports

Check for updates

OPEN

Sustainable synthesis of iron-doped manganese oxide nanoparticles for effective photo-accelerated detoxification of *tetracycline*

Sanjay S. Majani[1], M. A. Veena[2]✉, C. M. Hemanth Kumar[2], Poojitha B. Sridhara Setty[3], Muzaffar Iqbal[4], Chandan Shivamallu[5], Charley A. Cull[6], Kristin E. Hales[7], Paul R. Broadway[8], Raghavendra G. Amachawadi[9]✉ & Shiva Prasad Kollur[1]✉

The widespread use of antibiotics has severely impacted water bodies and ecosystems, necessitating well-designed photocatalysts for effective degradation. In this regard, present work reports the synthesis of MnO_2:xFe^{3+} (MF-x, x = 0, 2, 4, 6, 8, and 10) nanoparticles via the bio-mediated process using *Tridax procumbens* as the reducing and stabilizing agents. Various physicochemical approaches confirmed the structural, optical, and morphological properties of MF-x nanoparticles, revealing a reduced optical bandgap (2.06–0.97 eV) for visible-light photocatalysis. PXRD analysis reveals cubic crystalline nature of MF-x nanoparticles belonging to space group number 206 (I a-3) with crystallite sizes ranging 39–70 nm, which was further refined using Rietveld method with acceptable χ^2 value of 2.3 for the doped sample. Raman spectra confirmed the existence of F_g and $E_g + F_g$ active modes from the bixbyite structure corresponding to the space group I a-3. Furthermore, the FESEM and TEM analyses showed a highly crystalline uniform porous morphology with evaluated particle sizes in agreement with the PXRD results. Additionally, the quantitative aspects of precursor elements were confirmed through XPS studies. The photocatalytic activity of MF-10 in degrading Tetracycline hydrochloride (TC-HCl) was evaluated under optimized pH, catalyst dosage, and TC-HCl concentration under visible light. Results show that optimized weight (100 mg) of as-synthesized nanoparticles exhibit high photocatalytic performance with a 94.23% degradation against optimized 20 ppm TC-HCl in 90 min. On the other hand, pH variation and reusability test indicated that the degradation efficiency was significant at neutral pH and reduced at the 5th cycle (64.28) which was further authenticated by pH_{PZC} evaluation (7.55). Thus, the present work showcased the potential application of MnO_2: Fe^{3+} nanoparticles as low-cost and environmentally friendly material in water treatment applications.

Keywords Manganese Ferrites, *Tridax procumbens*, Photocatalysis, Tetracycline hydrochloride

The growing pollution of water bodies due to pharmaceutical contaminants, particularly antibiotics, has emerged as a significant environmental issue[1–5]. Phase 1 focuses on a group of widely used antibiotics from the tetracycline class. Among them, Tetracycline Hydrochloride (TC-HCl) is one of the most commonly detected

[1]School of Physical Sciences, Amrita Vishwa Vidyapeetham, Mysuru Campus, Mysuru, Karnataka 570 026, India. [2]Department in Chemistry, Chemistry Research Centre, Bangalore Institute of Technology, K.R. Road, VV Puram, Bangalore, Karnataka 560 004, India. [3]Department of Biotechnology, G.M. University, Davangere, Karnataka 577 006, India. [4]Department of Pharmaceutical Chemistry, College of Pharmacy, King Saud University, 11451 Riyadh, Saudi Arabia. [5]Department of Biotechnology and Bioinformatics, JSS Academy of Higher Education and Research, Mysuru, Karnataka 570 015, India. [6]Midwest Veterinary Services, Inc., Oakland, NE 68045, USA. [7]Department of Animal and Food Science, Texas Tech University, Lubbock, TX 79409, USA. [8]USDA-ARS Livestock Issues Research Unit, Lubbock, TX 79415, USA. [9]Department of Clinical Sciences, College of Veterinary Medicine, Kansas State University, Manhattan, KS 66506-5606, USA. ✉email: veenamdy12@gmail.com; agraghav@vet.ksu.edu; shivachemist@gmail.com

antibiotics in aquatic environments due to incomplete metabolism and improper disposal. Its persistence in water systems poses significant ecological risks, including the promotion of antibiotic-resistant bacteria, which threaten both environmental and public health. Consequently, the presence of TC-HCl in wastewater has garnered considerable scientific attention in recent years[6,7]. Photocatalysis is an advanced oxidation process, which has shown great potential for the degradation of recalcitrant organic contaminants, such as antibiotics[8–10].

Photocatalysts are vital for environmental remediation and energy uses, employing light-assisted reactions to power sustainable chemical processes[11]. They efficiently break down organic contaminants in wastewater, such as antibiotics and dyes, avoiding ecological damage and antimicrobial resistance[12]. Increasing water source contamination requires effective photocatalytic treatment. In addition to wastewater treatment, photocatalysts are important in air purification, hydrogen generation, and antimicrobial uses[13]. They are also utilized in self-cleaning surfaces, CO_2 mitigation, and chemical sensing. They are of significant importance in accelerating reactions when exposed to light, making them critical for green technology, advancing environmental sustainability, and advanced material research[14]. Hence, the design of advanced photocatalysts that are efficient, economical, and environmentally friendly is of utmost importance for tackling this challenge.

MnO_2 is one of the transition metal oxides that possess multiple polymorphs and has garnered interest as a photocatalyst. This compound, having outstanding redox properties[15] and environmental compatibility along with being abundant[16], finds considerable attention as a photocatalyst[17–19]. However, pristine MnO_2 often faces challenges of lower photocatalytic efficiency mainly because of its relatively higher electron–hole recombination rate and suboptimal light absorption. Various strategies have been developed to overcome such limitations. Some of the approaches adopted are doping with foreign ions, surface modification, and introduction of nanostructures. Doping MnO_2 with transition metal ions such as Fe^{3+} proved particularly effective in modulating electronic structure thereby enhancing charge carrier dynamics in promoting photocatalytic performance[20–22].

The introduction of Fe^{3+} into MnO_2 enhances its photoactivity. It possesses extra functionalities beyond this, i.e., stronger adsorption strength and extended photosensitivity into the visible region, making Fe^{3+}-doped MnO_2 a highly prospective material for application in the degradations of antibiotics. Recent researchers have found that Fe^{3+}-doped MnO_2 can be very effective in degrading many organic pollutants[23,24]. However, most of these materials are synthesized by conventional chemical routes that depend on the use of toxic reducing agents and extreme reaction conditions[25,26]. This is not only environmentally adverse but also problematic for sustainable and scalable production[27,28].

To overcome these drawbacks, green synthesis methods have become popular as an alternative to nanomaterial preparation. Bio-reduction, using plant extracts or other biological agents as reducing and stabilizing agents, is one of the promising routes for nanostructure synthesis with eco-friendliness and sustainability[29]. Using plant extracts to synthesize photocatalysts enhances their physicochemical properties by introducing bioactive compounds that help achieve controlled morphology, improved crystallinity, and increased surface area, which are vital for efficient light absorption and separation of charge carriers[30]. Additionally, the addition of phytochemicals influences defect states and oxygen vacancies, leading to greater photocatalytic performance due to improved dynamics of electron–hole pairs and the formation of reactive species[31,32]. One of the main advantages of using plant extracts is that they are rich in phytochemicals such as flavonoids, phenolic acids, and alkaloids, which act naturally as reducing agents[33,34]. This approach eliminates the need for toxic chemicals, conserves energy, and aligns with the principles of green chemistry. Furthermore, nanomaterials synthesized through this method possess unique physicochemical properties, such as increased surface area and improved crystallinity, making them highly valuable for catalytic applications.

Among various potential candidates, *Tridax procumbens* was selected for its rich phytochemical composition and well-documented biological properties (Table S1). *Tridax procumbens*, commonly known as coat buttons, is a medicinal plant widely distributed in tropical and subtropical regions. Its extracts are rich in flavonoids, tannins, saponins, and phenolic compounds, which not only serve as reducing agents but also contribute to the degradation of organic pollutants through additional reactive oxygen species (ROS) generation[35,36]. Flavonoids and phenolic acids are known to enhance the photocatalytic activity of nanomaterials by stabilizing the nanoparticles and facilitating charge transfer. The antimicrobial and antioxidant properties of *Tridax procumbens* further enhance its utility in wastewater treatment, making it an ideal choice for the green synthesis of photocatalysts[37–39]. Detailed information on all the bio-active compounds plausibly present in *Tridax procumbens* is extracted from the database by James A. Duke[40].

This research presents the pioneering use of *Tridax procumbens* leaf extract as a novel bio-reducing agent in the green synthesis of Fe^{3+}-doped MnO_2 nanostructures, establishing an eco-friendly and sustainable approach for nanomaterial fabrication. The as-synthesized MnO_2: Fe^{3+} nanostructures exhibited remarkable photocatalytic efficiency in the degradation of Tetracycline, highlighting their potential for applications in wastewater treatment. The enhanced degradation performance is attributed to the synergistic effects of Fe^{3+} doping combined with the unique physicochemical properties imparted by the green synthesis method. This study expands the possibilities for bio-inspired nanomaterial synthesis and provides a sustainable strategy to address antibiotic contamination in aquatic environments.

Experiments

Materials and methods

All chemicals required to perform the present study were purchased from commercial vendors and used without further purification unless specified; Manganous (II) acetate tetrahydrate ($(CH_3COO)_2Mn \cdot 4H_2O$) (Merck, ≥ 98%) and Ferric (III) nitrate nonahydrate ($Fe(NO_3)_3 \cdot 9H_2O$) (Merck, ≥ 98%) and Deionised water (Merck Millipore). Structural, morphological, optical, and surface characteristics of as-synthesized nanoparticles were investigated by employing different sophisticated techniques. Phase purity and crystal structure were analyzed by powder X-ray diffraction (PXRD) with the help of a Bruker D8 Advance diffractometer. Surface functional

groups were determined by Fourier transform infrared (FTIR) spectroscopy with the aid of a SHIMADZU IRTracer-100. Optical characteristics, such as band-gap analysis, were investigated by employing a SHIMADZU UV 3600 PLUS UV–Vis spectrophotometer. Raman spectral analysis was conducted on a WITec Alpha 300RA Raman spectrometer. The morphological features and elemental composition were examined using field emission scanning electron microscopy (FESEM) and energy-dispersive X-ray spectroscopy (EDS) on a TESCAN MAIA3 XMH microscope. Transmission electron microscopy (TEM) was carried out on a JOEL JEM-2100 instrument to identify the particle size and lattice fringes. The magnetic characteristics were studied on a Lake Shore 8600 Series vibrating sample magnetometer (VSM). X-ray photoelectron spectroscopy (XPS) was conducted on a PHI Genesis Fully Automated Multi-Technique Scanning XPS/HAXPES Microprobe from Physical Electronics to study the oxidation states and surface chemical composition. The Brunauer–Emmett–Teller (BET) surface area and porosity were measured with an Autosorb iQ-x instrument from Quantachrome. Furthermore, the total organic carbon (TOC) concentration was measured through the use of a SHIMADZU TOC-L Series analyzer.

The characterization data were analyzed using various software tools to ensure accurate interpretation. The PXRD data were analyzed using HighScore Plus 3.0.5, PANalytic B.V. Almelo, The Netherlands (https://www.malvernpanalytical.com/en/products/category/software/x-ray-diffraction software/highscore-with-plus-option.). Rietveld Refinements were performed through FullProf Suite[41]. FESEM and TEM images were analyzed for morphology using ImageJ, a free software (https://imagej.net/ij/index.html). All the RAW data from the characterization was analyzed and processed for graphical representation using OriginPro, Version 2024. OriginLab Corporation, Northampton, MA, USA.

Collection of *Tridax procumbens* leaves

With the help of a botanist, healthy *T. procumbens* leaves were collected from agricultural fields near Tavarekere, Bangalore, Karnataka, India that are regionally identified as Addike soppu/Attige soppu/Gabbu sanna shavanthi/Netta gabbu shavanthi. Selected leaves were separated, and washed with sterile distilled water to remove the surface adhered dust particles, ensuing taxonomical authentication by a Botanist. Collected leaves were then shade-dried in a dust-free environment overnight to remove moisture.

Preparation of *Tridax procumbens* leaf extract

The *Tridax procumbens* L. extract was prepared as described in our previous work[42]. Twenty-five grams (25 g) of shade-dried *Tridax procumbens* leaves were suspended in 150 mL of double distilled water taken in a 250 mL conical flask and boiled to 80 °C for about 30 min until the water was reduced to half of its initial volume. The resulting greenish brown extract was cooled and filtered through Whatman filter paper No. 1. Obtained filtrate was stored in a sealed container under 4 °C until further use.

Synthesis of pristine MnO_2 and MnO_2:Fe^{3+} NPs using *Tridax procumbens* leaf extract

Synthesis of MnO_2: xFe^{3+} (x = 0.2 mmol) nanoparticles was carried out via the green synthetic route using *Tridax procumbens* leaf extract as similarly described in[43]. Stoichiometric quantities of manganese (II) acetate tetrahydrate (2.4018 g) (Merck, ≥ 98%) (9.7 mM) and iron (III) nitrate nonahydrate (0.0808 g) (Merck, ≥ 98%) (0.2 mM) were dissolved in 100 mL of deionized water. To this, the prepared plant extract was added dropwise under constant stirring. The mixture was heated at 80 °C with continuous stirring until the colour changed from greenish red to brownish black. This change indicated the completion of doping and the formation of nanoparticles. The obtained nanoparticles were then subjected to centrifugation at 10,000 rpm for 15 min at room temperature. Further washed with absolute ethanol (3×) to remove any unbound materials, dried in an oven at 80 °C for 4 h and calcined at 600 °C for an additional 3 h, resulting in brownish-black nano oxides. Once cooled to room temperature, the obtained nano oxide was designated as MF-2. A similar method was used to obtain pristine MnO_2 nanoparticles and a series of Fe-doped MnO_2 nanoparticles with different ratios of $Fe(NO_3)_3 \cdot 9H_2O$ (0.0, 0.4, 0.6, 0.8, and 1.0 mmol), and samples were abbreviated as MF-0, MF-4, MF-6, MF-8, and MF-10, respectively. Detailed information about the precursor quantities is tabulated in Table 1.

Antibiotic degradation

The catalytic efficiency of the prepared MF-10 sample under visible light irradiation in degrading TC-HCl was evaluated using the degradation set-up equipped with a 150 W metal halide lamp with ~ 2600 W/m^2 irradiance. Initially, the experiment starts with preparing 3 distinct 20 ppm (20 mg/L) TC-HCl solutions using doubly-distilled water and mixing it with a properly weighed selected photocatalyst, MF-10 samples in respective concentrations of 50 mg, 75 mg, and 100 mg. The mixture was then allowed to acquire adsorption–

Sample abbreviation	Wt. of $C_4H_6MnO_4 \cdot H_2O$ (in grams)	Wt. of $Fe(NO)_3 \cdot 9H_2O$ (in grams)	Mole ratio	Percentage	
				Mn	Fe
MF-0	2.4509	0.0000	0.01:0.00	100	0
MF-2	2.4018	0.0808	0.0097:0.0002	98	2
MF-4	2.3528	0.1616	0.0095:0.0004	96	4
MF-6	2.3038	0.2424	0.0093:0.0006	94	6
MF-8	2.2548	0.3232	0.0091:0.0008	92	8
MF-10	2.2058	0.4040	0.0089:0.001	90	10

Table 1. Quantitative information of precursor quantities.

desorption equilibrium in the dark for 30 min. Further, the mixture was illuminated with visible light with the wavelength > 420 nm from all directions. 2.5 mL of mixture solution was pipetted out every 10 min and centrifuged at 8000 rpm to record the UV–visible spectrum and study the characteristic wavelength at 361 nm. Furthermore, the recorded spectra were utilized in evaluating the degradation efficiency using the relation (1)[44],

$$Effeciency\,(\%) = \left(\frac{A_0 - A_t}{A_0}\right) \times 100 \quad (1)$$

where A_0 and A_t indicate initial absorbance and absorbance at a particular time t. Similar procedure were employed in evaluating the mechanism by conducting trapper test. Scavengers like Na_2SO_4, $C_6H_8O_6$ (ascorbic acid), TEOH (triethanolamine), methanol, and isopropanol were used in distinct degradation solution to evaluate the degradation rate. Further, reusability of the recovered photocatalyst was checked every cycle until recycled for the 5th time.

Results and discussion

Band-gap studies

Electronic transitions and band gap evaluations were done by recording the UV–visible (UV–vis) absorption spectra of the synthesized pristine MnO_2 and Fe^{3+}-doped MnO_2 nanoparticles over a range of 200–1200 nm. The absorption spectrum of pristine MF0 (Fig. 1A) showed a broad peak at around 265–480 nm, which was attributed to the charge transfer transitions involving the Oxygen 2p orbitals in the valence band and Manganese 3d orbitals in the conduction band. The most pronounced absorption in this range is assigned to oxygen-to-manganese charge transfer prevailing in this wavelength range and showing an efficient photoexcitation of electrons from the valence to the conduction band[45].

Doping with Fe^{3+} ions caused significant changes in the absorption spectrum. Except for the MF0 absorption, samples MF-2 to MF-10 had another band extending into the visible region; the onset is slightly red-shifted for the doped sample compared to the pristine MnO_2 sample. The shift might be caused by mid-gap defect states brought by Fe^{3+} ions which allow further electronic transitions. These mid-gap states allow both metal-to-metal charge transfer transitions (Mn → Fe) and d-d transitions within the Fe^{3+} ions, which together enhance the absorption in the visible region. The red-shift and broadening of the absorption band indicate a reduction in the bandgap energy from 2.06 to 0.97 eV after Fe^{3+} doping as observed in Fig. 1B[46]. The obtained results

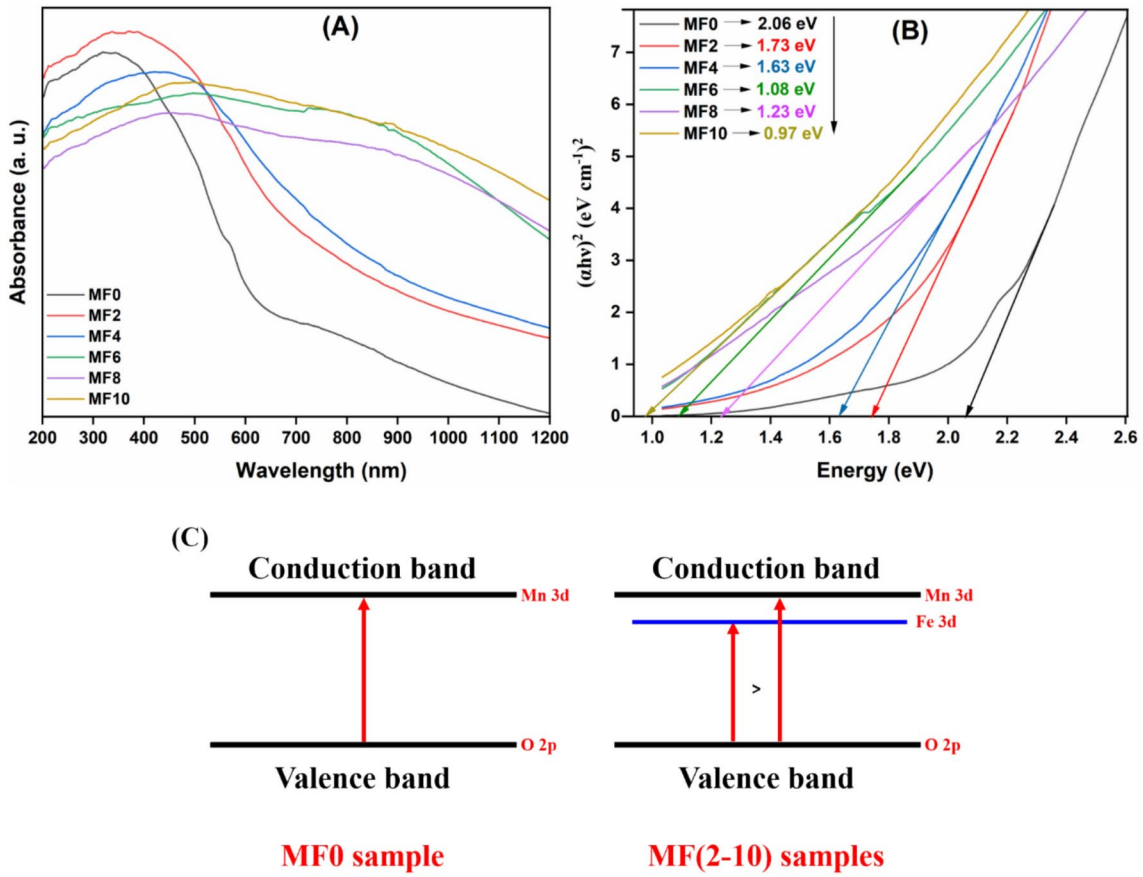

Fig. 1. (**A**) UV–Visible absorption spectra of MF (0–10) samples, (**B**) corresponding Tauc plot evaluating band gap energies, and (**C**) transition mechanism responsible for absorption band of MF (0–10) samples.

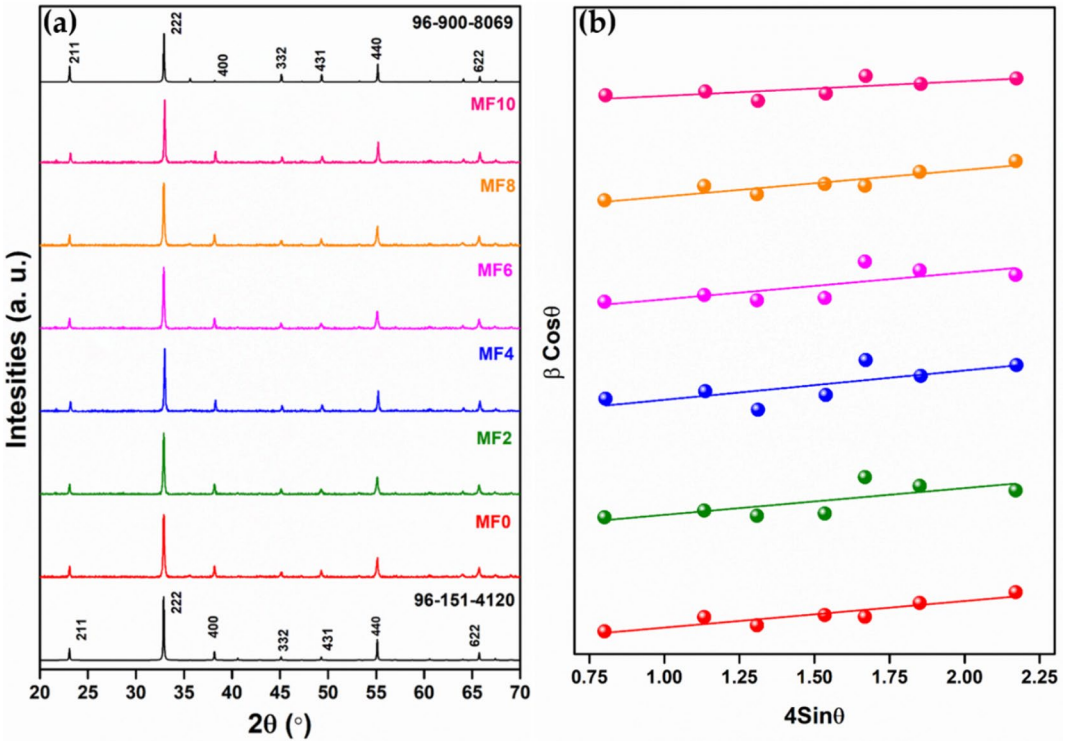

Fig. 2. (**a**) PXRD patterns of MnO_2: xFe^{3+} (x = 0, 2, 4, 6, 8, and 10 mol%) aligning with pristine and Fe^{3+} doped Manganese Oxide cards, #96-151-4120 and 96-900-8069, respectively. (**b**) W–H Plot of MnO_2: xFe^{3+} (x = 0, 2, 4, 6, 8, and 10 mol%).

Parameters	Values	
	#96-151-4120 (MF-0)	#96-900-8069 (MF-10)
Crystal system	Cubic	Cubic
Space group	I a-3	I a-3
Space group number	206	206
α (°)	90	90
β (°)	90	90
γ (°)	90	90
a (Å)	9.4080	9.4000
b (Å)	9.4080	9.4000
c (Å)	9.4080	9.4000

Table 2. Lattice parameters information from phase attainment analysis.

of decrement in band-gap with increasing Fe3 + concentration was well aligned with the reported results[47,48]. The detailed electronic transition mechanism is shown in Fig. 1C. This, in turn, implies Fe^{3+} doped MnO_2 nanoparticles can use a larger segment of the solar spectrum making them suitable for photocatalytic and optoelectronic applications. Electronic defect states through Fe^{3+} aptly modify the electronic structure thus enhancing the material's ability to absorb visible light and therefore optoelectronics performance under various multifunctional applications.

Structural assessments

Structural assessments for the as-prepared samples were done by recording PXRD spectra between the 2θ range of 20° and 70°. Figure 2a demonstrates the PXRD patterns MF-(0-10) samples exhibiting a perfect match for JCPDS file #96-151-4120 for MF-0 and #96-900-8069 for MF-10. The phase attainment results reveal that there is no major change in the phase before and after incorporating the Fe^{3+} ions into the host MnO_2. All the as-prepared samples exhibited a perfect match with the cubic phase. The lattice parameters of MF-0 and MF-10 samples are tabulated in Table 2, which show no major change but a slight variation in unit-cell lengths. Variations in lattice parameters of MF-2, MF-4, MF-6, and MF-8 samples are exhibited in Table S1. Major peaks detected at 2θ = 23.00°, 32.77°, 38.15°, 45.09°, 49.33°, 55.13°, and 65.76° were assigned with (211), (222), (400),

(332), (431), (440), and (622) hkl values, respectively. The average crystallite sizes of each sample were evaluated by substituting the same obtained peak values in Scherrer's relation (2)[49]:

$$D_c = \frac{0.9\lambda}{\beta_{hkl}\cos\theta} \tag{2}$$

where 0.9, is the shape factor on assuming circular shape, D_c, λ, and β_{hkl} refer to crystallite size, wavelength of the X-rays used, and Full Width at Half Maximum (FWHM) of the selected peaks. The evaluated results show a crystallite size range of 39–74 nm. The same was affirmed in plotting the Williamson-Hall relation (3)[50] for each pristine and doped sample as depicted in Fig. 2b.

$$\beta_{hkl}\cos\theta = \frac{0.9\lambda}{D_c} + 4\varepsilon\sin\theta \tag{3}$$

where ε refers to the strain component. The results are tabulated in Table 3, affirming a significant increment in the crystallite size after incorporating the Fe^{3+} ions at the Mn^{2+} sites. The rationale behind this increment is lattice strain relaxation, where strain created upon incorporating the Fe^{3+} ions is saturated with the increment in the crystallite size[51]. The same was observed in the strain component.

For more quantitative phase information of the samples, Rietveld refinement[52] was conducted using FullProf suite software utilizing the ***JCPDS*** file #96-151-4120 for MF-0 and #96-900-8069 for MF-10. Figure 3a and b show good agreement with the selected ***JCPDS*** files for the respective samples' PXRD pattern with the refinement parameters tabulated in Table 4. Figure 3c and d represent the extracted structure of MF-0 and MF-10 samples using Diamond-5 software.

Furthermore, for extended information about the electron distribution inside the unit cell, the GFourier tool in FullProf was utilized in mapping electrons. This analysis, performing Fourier Transforms on structural factors throughout the unit cell, presents the atomic locations inside the unit cell. Figure 4 depicts the 2D and 3D electron density mapping of the prepared MF-0 and MF-10 samples.

Raman analysis

Raman analysis, an efficient technique used for more insights about the vibrational properties of the materials, was utilized to record the spectrum of prepared pristine and Fe^{3+} doped MnO_2 nanoparticles. The bixbyite structural type matching with the PXRD data has a cubic phase with Ia-3 space group and 22 Raman active modes with the description of $4A_g + 4E_g + 14F_g$, 10 inactive modes $5A_u + 5E_u$, and 16 T_u IR modes. With so many Raman active modes (22), the number of modes appearing in the Raman spectrum is reduced[53]. Figure 5 shows the spectrum ranging between 100 and 1600 cm^{-1} Raman shift revealing the prominent strong and weak bands at 632.43 cm^{-1} and 313 cm^{-1}. Considering the above-discussed crystallographic symmetry, the bixbyite structural type explains all the Raman active modes in the spectrum consistent with the result obtained from XRD. Bands are broad too, which contradicts the expectation since the calculated crystallite size is larger as discussed in the PXRD section. The characteristic bands observed at 632.43 cm^{-1} and 313 cm^{-1} correspond to F_g and $E_g + F_g$ modes linking to Mn–O vibrations as labeled in the Fig. 5. Furthermore, the presence of Fe^{3+} in the structure is highlighted by the peak broadening observed in the spectrum attributed to the changes in the force constants and vibrational amplitudes of neighboring peaks[54,55].

Magnetic properties

Measurements using vibrating sample magnetometry (VSM) were used to examine the magnetic characteristics of the nanoparticles, including remanence, coercivity, and saturation magnetization. The hysteresis loop (Fig. 6), obtained for the MF-10 sample from the VSM analysis, showed a remnant magnetization (Mr) of 33.42 emu/g and a saturation magnetization (Ms) of 65.11 emu/g at 15 kOe. This validated the nanoparticles' strong magnetic properties. A coercivity (Hc) value of 1393.47 Oe demonstrated their susceptibility to external magnetic fields, with the detection of reversible magnetization transformations[56,57]. Further, the high magnetic property of the MF-10 sample is demonstrated in the supplementary file GIF. S1.

Morphology

Figure 7a–h represents the FESEM images of prepared MF-0 (a–d) and MF-10 (e–h) extending over 2 µm to 500 nm magnification range. As seen in the images the MF0 sample exhibits a network-like morphology

Sample	Crystallite size (nm)		Strain component (ε)	Band gap energy (E_g) (in eV)
	Scherrer's	WH Plot		
MF-0	39.92	42.16	0.02722	2.06
MF-2	60.21	63.47	0.04964	1.73
MF-4	73.37	75.12	0.04722	1.63
MF-6	68.24	70.28	0.04829	1.08
MF-8	62.86	65.18	0.04867	1.23
MF-10	70.13	72.68	0.04926	0.97

Table 3. Crystallite size, strain, and Refractive index evaluation of prepared samples.

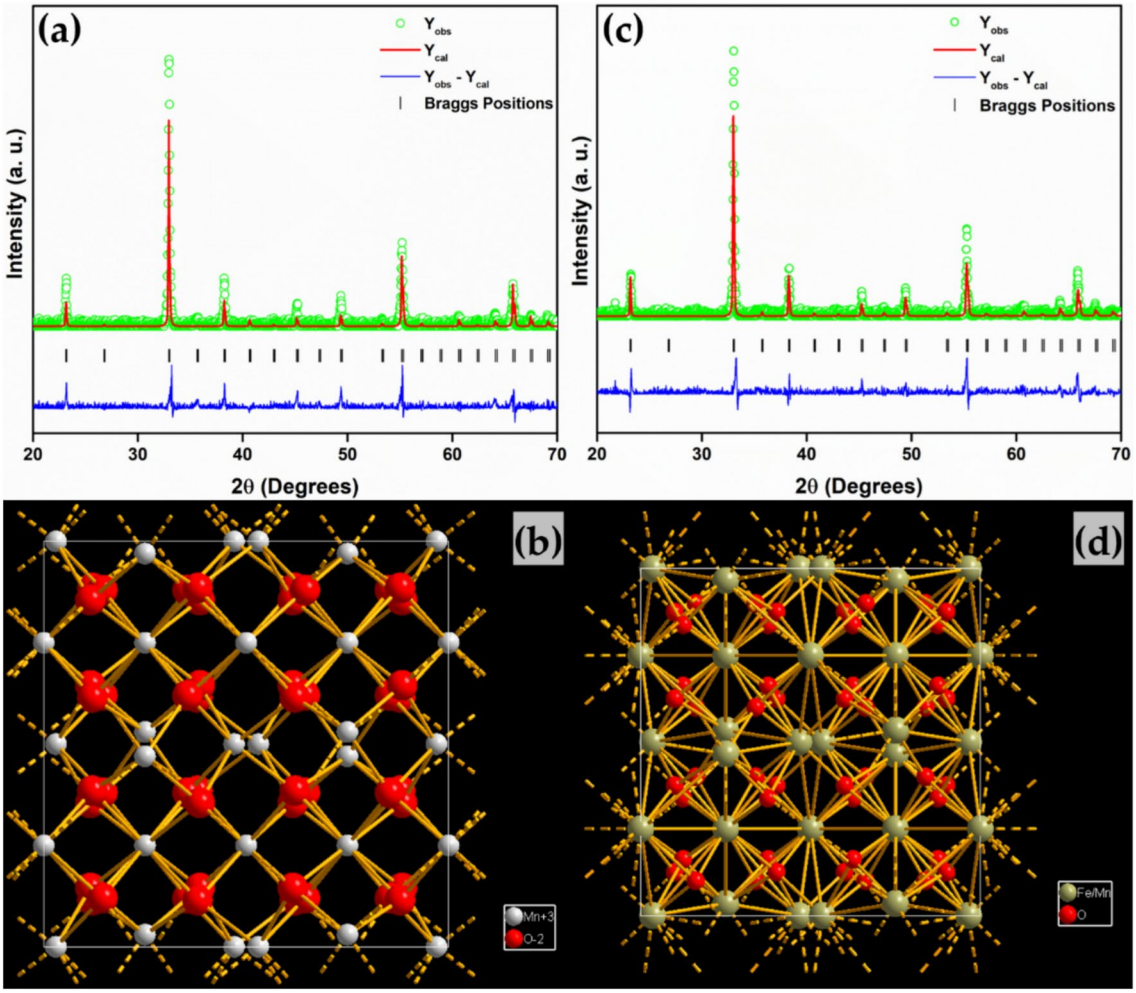

Fig. 3. Rietveld refinement and extracted crystal structure of (**a**, **b**) MnO_2 and (**c**, **d**) MnO_2: 10 mol% Fe^{3+} samples.

Refinement parameters	#96-151-4120 (MF-0)	#96-900-8069 (MF-10)
R_p	75.2	73.7
R_{wp}	81.5	80.0
R_{exp}	47.85	52.75
χ^2	2.9	2.3
GOF	1.70	1.51

Table 4. Phase refinements parameters from the Rietveld method.

consisting of various shapes with a particle size averaging at ~39 nm (Fig. 7i). After incorporating Fe^{3+} ions into the MnO_2, the MF10 sample exhibits a porous network-like morphology with an averaging particle size at ~71 nm (Fig. 7j). The significant porotic changes to the morphology can be aligned with the successful incorporation of Fe^{3+} ions. Furthermore, a prominent qualitative elemental analysis over a selected area of MF0 and MF10 samples was conducted and imaged as it is in Fig. 8A and B, respectively. The results observed affirm the precursor elements with a Gold (Au) contamination from the sputtering process.

Also, confirming the morphology and crystallinity, TEM analysis was conducted on the MF10 sample as depicted in Fig. 9a–h. TEM images affirm the different shapes (rod, smooth-edge cube, and sharp crystal-end) networked morphology which aligns with FESEM results. Lattice spacing and crystallinity were also assured through HRTEM and SAED images as depicted in Fig. 9g and h, respectively.

Surface area analysis

The MF-10 sample was evaluated for its surface area, pore volume, and pore size through BET surface area analysis conducted at 160 °C for 2 h. In Fig. 10a, the adsorption/desorption isotherm curve is displayed

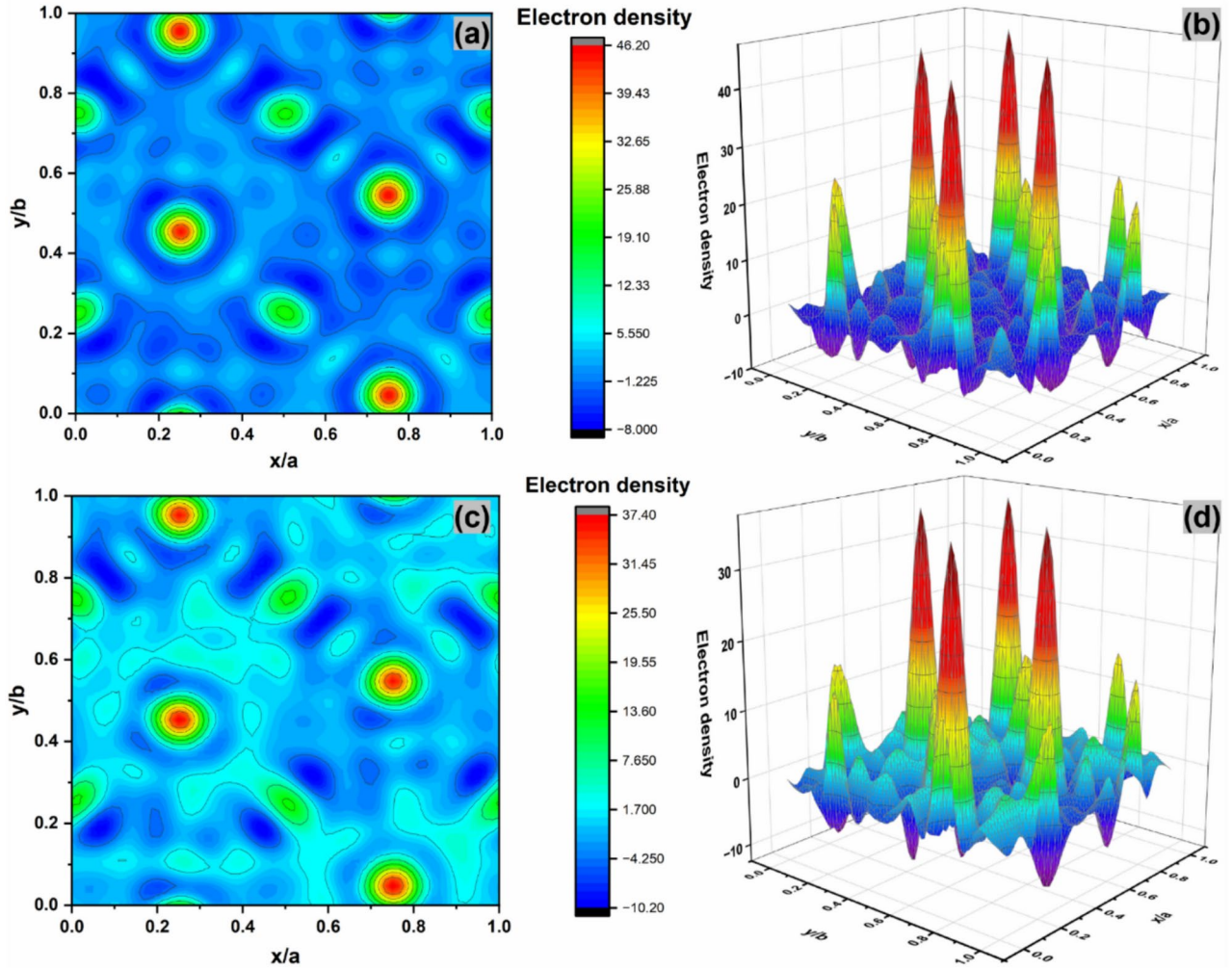

Fig. 4. (**a**, **b**) and (**c**, **d**) 2D and 3D electron density map in the unit cell of MnO_2 and MnO_2: 10 mol% Fe^{3+} samples, respectively.

alongside the pore size distribution of the synthesized MF-10 sample. The N_2 adsorption and desorption data confirmed that the material exhibits a type II isotherm with an H_3 hysteresis loop, aligning with the classification established by the International Union of Pure and Applied Chemistry (IUPAC)[58]. This indicates the sample's mesoporous characteristics. Figure 10b depicts the determined BET surface area, average pore radius, and overall pore volume were recorded as 19,853 m^2/g, 3.691 nm, and 0.043 cm^3/g, respectively. According to IUPAC standards, porous materials are classified according to their pore size (d) as microporous ($d < 2$ nm), mesoporous (2 nm $< d <$ 50 nm), and macroporous ($d >$ 50 nm)[59]. Figure 10c illustrates the pore size distribution, which highlights a significant peak at 3.691 nm, further confirming the material's mesoporous nature.

Surface composition analysis

XPS measurements were done on the MF-10 sample to examine the quantitative chemical composition and oxidation states of the precursor elements. Figure 11a depicts the recorded XPS survey spectra between the binding energy range of − 10 to 1350 eV, affirming all the precursor elements in the sample. Furthermore, the Shirley-type background function was utilized in deconvoluting the high-resolution peaks of the respective elements.

As illustrated in Fig. 11b, the fit of the Mn 2p core-level high-resolution XPS spectra contains two distinct peaks: those at 641.51 eV and 653.18 eV. The Mn $2p_{3/2}$ and Mn $2p_{1/2}$ peaks occur at about 641.0 eV and 652.4 eV binding energies, respectively, and indicate Mn^{3+} ions with a spin–orbit splitting of approximately 11.4 eV. Figure 11c presents a high-resolution Fe 2p spectrum, which also distinctly depicts the Fe $2p_{1/2}$ and Fe $2p_{3/2}$ photoelectron peaks of two different oxidation states. Spectrum fitting was optimized on two PL for each Fe 2p component deconvoluted into a combination of Gaussian–Lorentzian peak lines. The resulting doublets had BEs at 710.87 eV and 724.44 eV, attributing to Fe $2p_{1/2}$ and Fe $2p_{3/2}$, respectively. Furthermore, high-resolution O 1 s and C 1 s show their respective prominence peaks at 729.72 eV and 284.72 eV, as depicted in Fig. 11d and e[60,61].

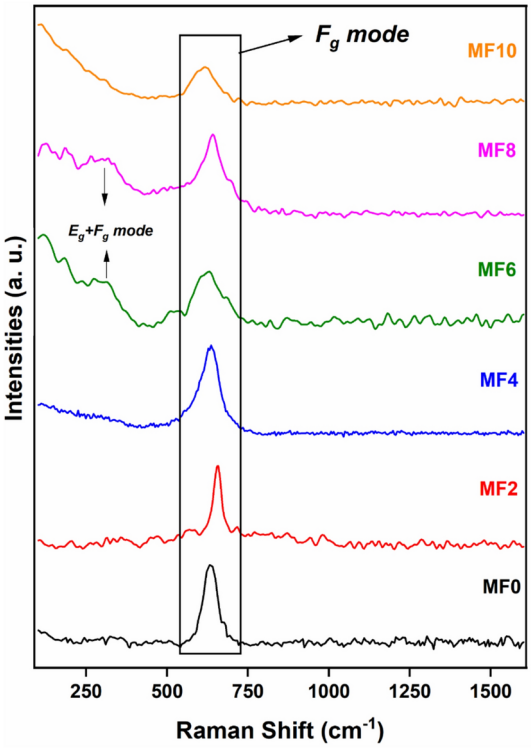

Fig. 5. Recorded Raman spectra of MnO_2: xFe^{3+} (x = 0, 2, 4, 6, 8, and 10 mol%) samples.

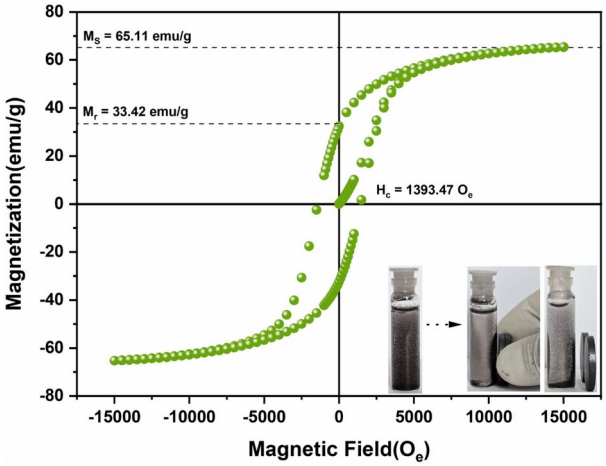

Fig. 6. Recorded hysteresis curve of MF-10 sample from VSM analysis.

Degradation of TC-HCl antibiotic

As mentioned in the experiments section, TC-HCl antibiotic degradation was conducted in a series of experiments. Figure 12a depicts the photocatalyst dosage effect on the degrading efficiency (%) of TC-HCl from the solution. The results yielded the efficiency (%) of 74.86%, 84.87%, and 94.23% for 50 mg, 75 mg, and 100 mg proportions, respectively after 90 min of visible light irradiation. The same results were analyzed for degradation kinetics using the pseudo-1st-order relation[62],

$$\ln\left(\frac{A_0}{A_t}\right) = k_1 t \tag{4}$$

where A_0 and A_t indicate initial absorbance and absorbance at a particular time t. k_1 refers to the rate constant of the 1st-order reaction. The degradation results suggest a good agreement with the selected 1st-order kinetics (Fig. 12b) with the parameters listed in Table 5.

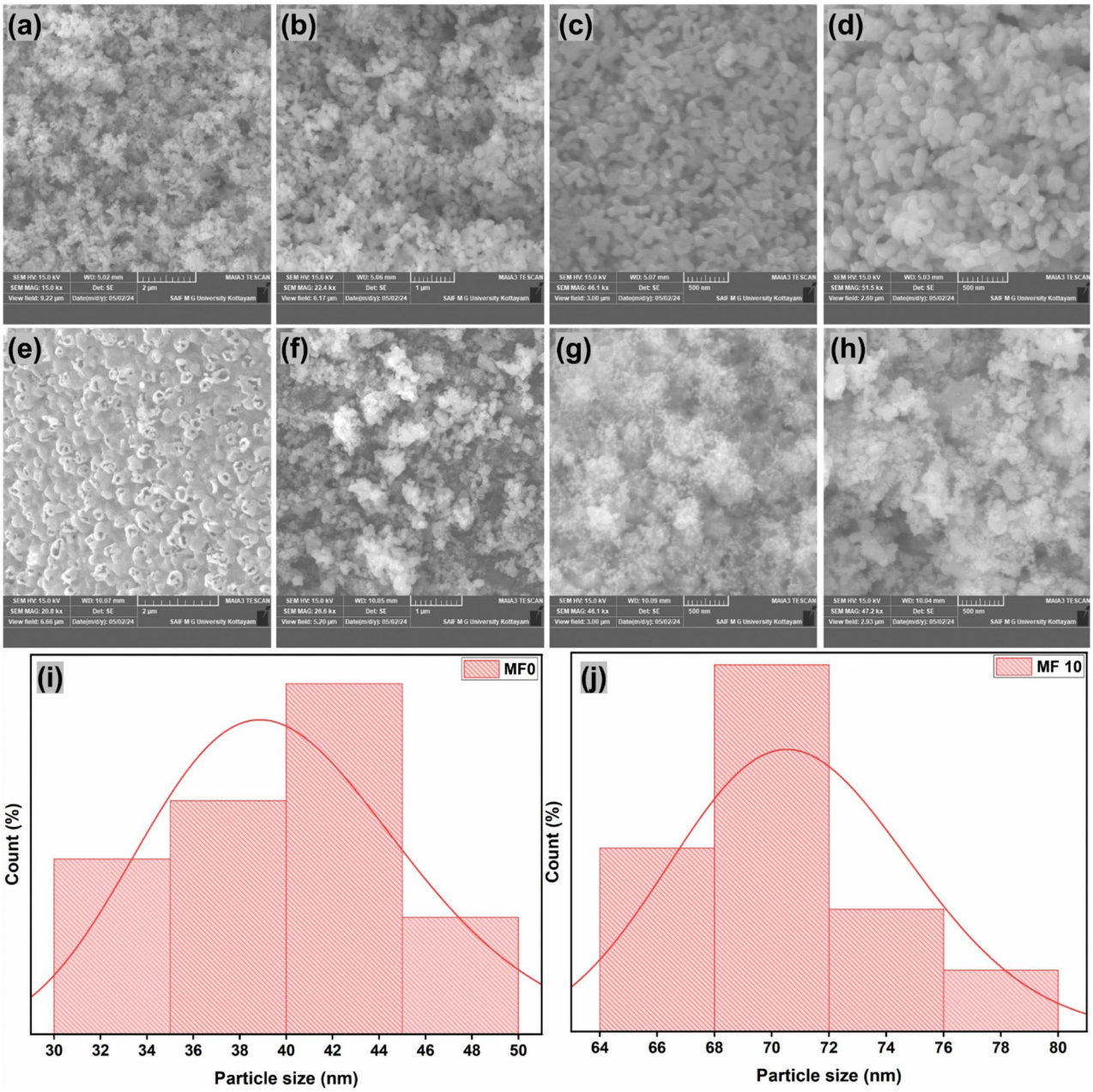

Fig. 7. FESEM images of pristine MnO_2 (**a**–**d**) and MnO_2: 10 mol% Fe^{3+} (**e**–**h**) samples at 2 µm, 1 µm, and 500 nm magnifications. (**i**, **j**) Long-normal particle size distribution curve of MF0 and MF10, respectively.

pH_{PZC} and trapper evaluation

The pH drift method was adopted to determine the pH_{PZC} of the as-prepared MF-10 sample in the presence of 0.1N NaCl electrolyte solution[63]. The pH of the solution was varied stepwise between 2 and 12 with the help of 0.1N NaOH and 0.1N HCl solutions. 50 mL of 0.1 N NaCl was filled in a conical flask with 0.10 g of MF-10 sample. This mixture was shaken at 150 rpm for 24 h to attain pH equilibrium. The difference (ΔpH) in the pH values obtained between the final and initial (pHi) values was plotted against the initial pH values. The pH_{PZC} value was determined from the x-axis intersection of this curve[64]. Figure 12c indicates that the pH_{PZC} of MF-10 is 7.55.

The trapper test was employed for the determination of reactive species participating in the photocatalytic reaction using scavengers like Na_2SO_4, $C_6H_8O_6$ (ascorbic acid), TEOH (triethanolamine), methanol, and isopropanol[45]. The selective additives of the reactants utilized as scavengers assist in quenching some ROS or radicals in the photocatalytic reaction process. In the current study, Na_2SO_4 was an electron scavenger, ascorbic acid a quencher of superoxide radicals ($\bullet O_2^-$), and TEOH, methanol, and isopropanol as hole (h^+) and hydroxyl radicals (•OH) traps, respectively. The test was performed by introducing a known quantity of each scavenger into the photocatalytic system under identical conditions, with subsequent monitoring of the

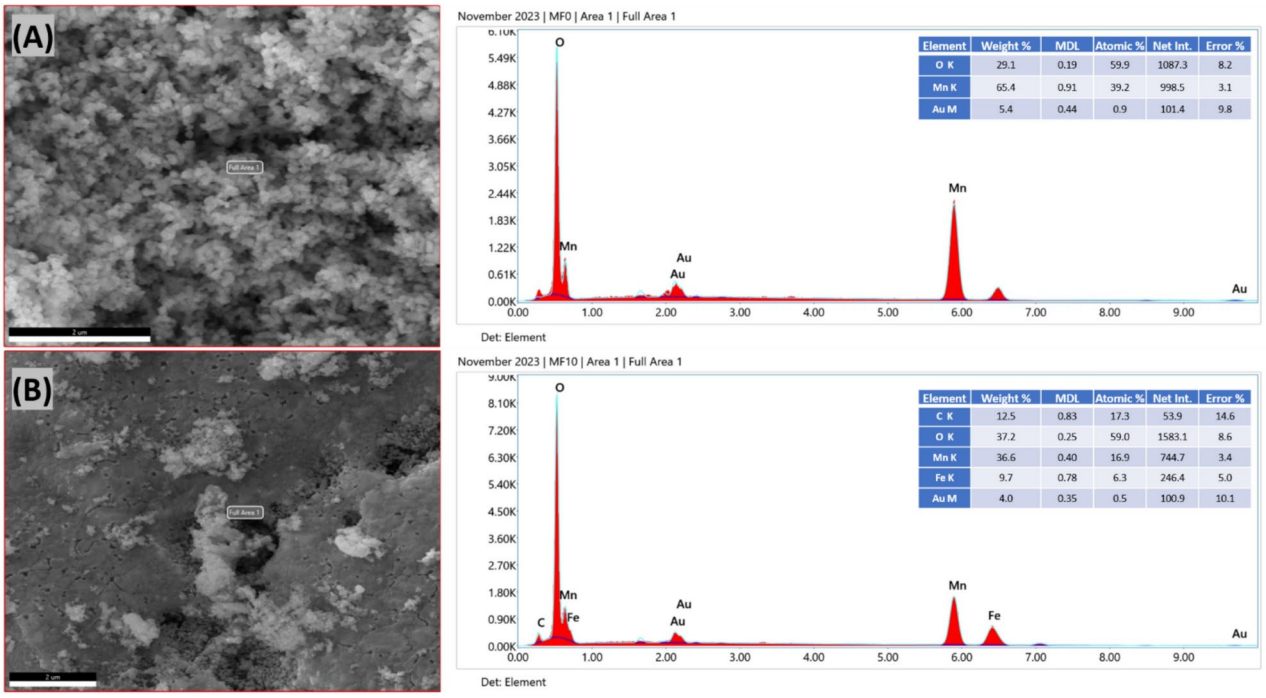

Fig. 8. Scanned area for elemental analysis and its corresponding EDAX spectrum of MnO_2 (**A**) and MnO_2: 10 mol% Fe^{3+} (B) samples.

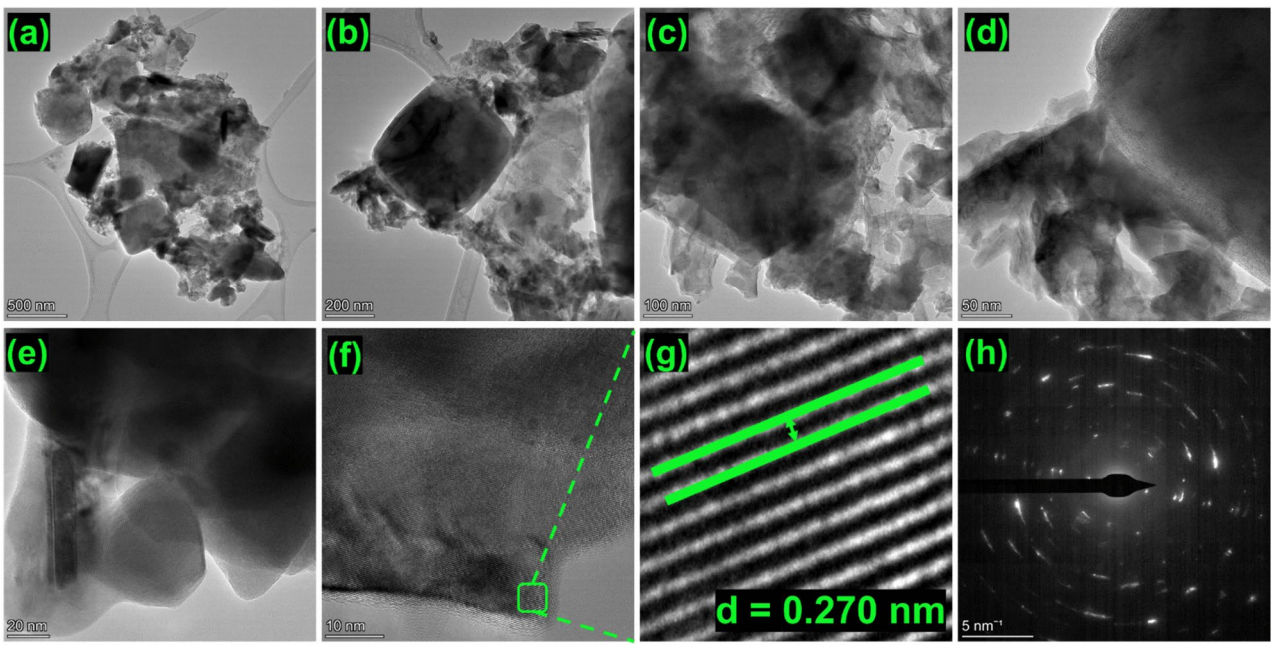

Fig. 9. TEM images of as-prepared MnO_2: 10 mol% Fe^{3+} sample at (**a**–**e**) 500 nm, 200 nm, 100 nm, 50 nm, and 20 nm magnification, respectively, (**f**, **e**) HRTEM images, and (**h**) SAED image.

effect on photocatalytic degradation efficiency. The results observed in Fig. 12d revealed the maximum effect on degradation efficiency was observed for ascorbic acid, suggesting the primary suspect as $\bullet O_2^-$ responsible for the photocatalytic degradation of TC-HCl.

pH variation and reusability test

The influence of the variation in pH on the photodegradation efficacy of TC-HCl was studied to understand the conditions of acidic, neutral, and basic pH variations on the photocatalytic degradation reaction. It was

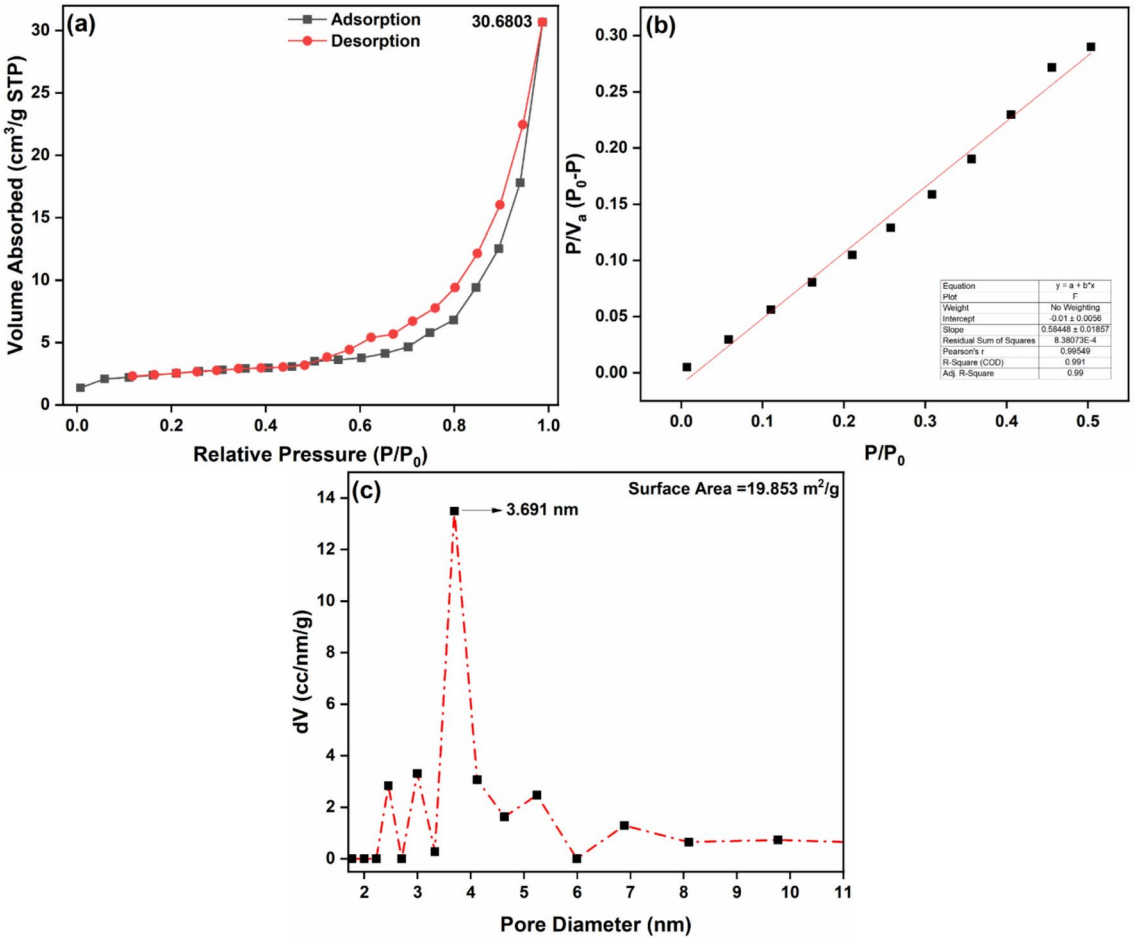

Fig. 10. (**a**) N_2 adsorption–desorption isotherm curve, (**b**) BET adsorption plot, and (**c**) pore size distribution curve of as-obtained MF-10 sample.

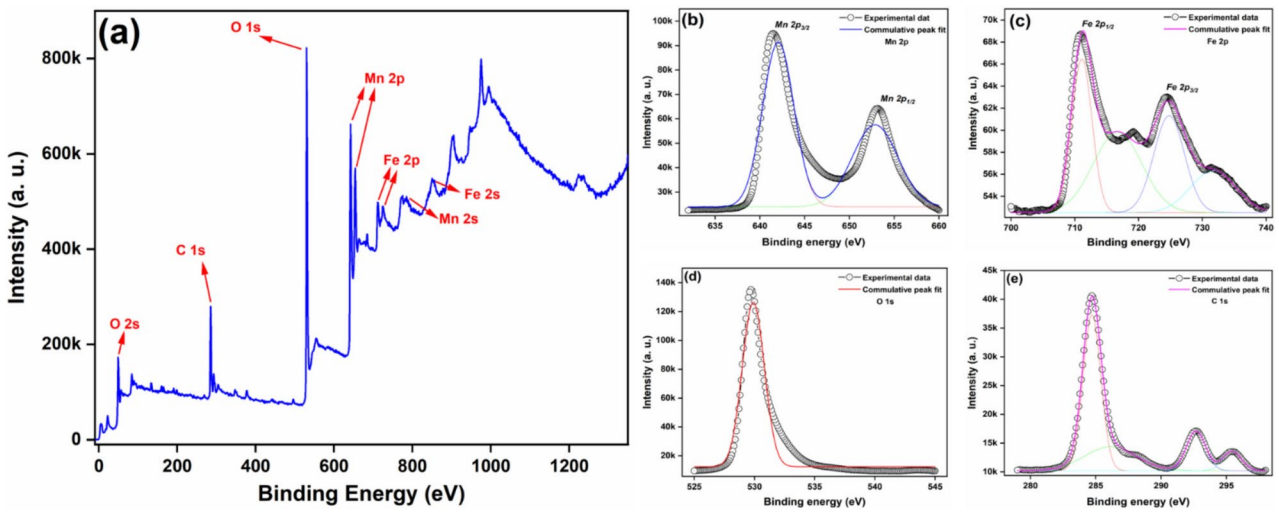

Fig. 11. Qualitative and Quantitative elemental XPS analysis of as-prepared MnO_2: 10 mol% Fe^{3+} sample. (**a**) Overall spectra and (**b**–**e**) deconvoluted individual Mn 2p, Fe 2p, O 1s, and C 1s peaks.

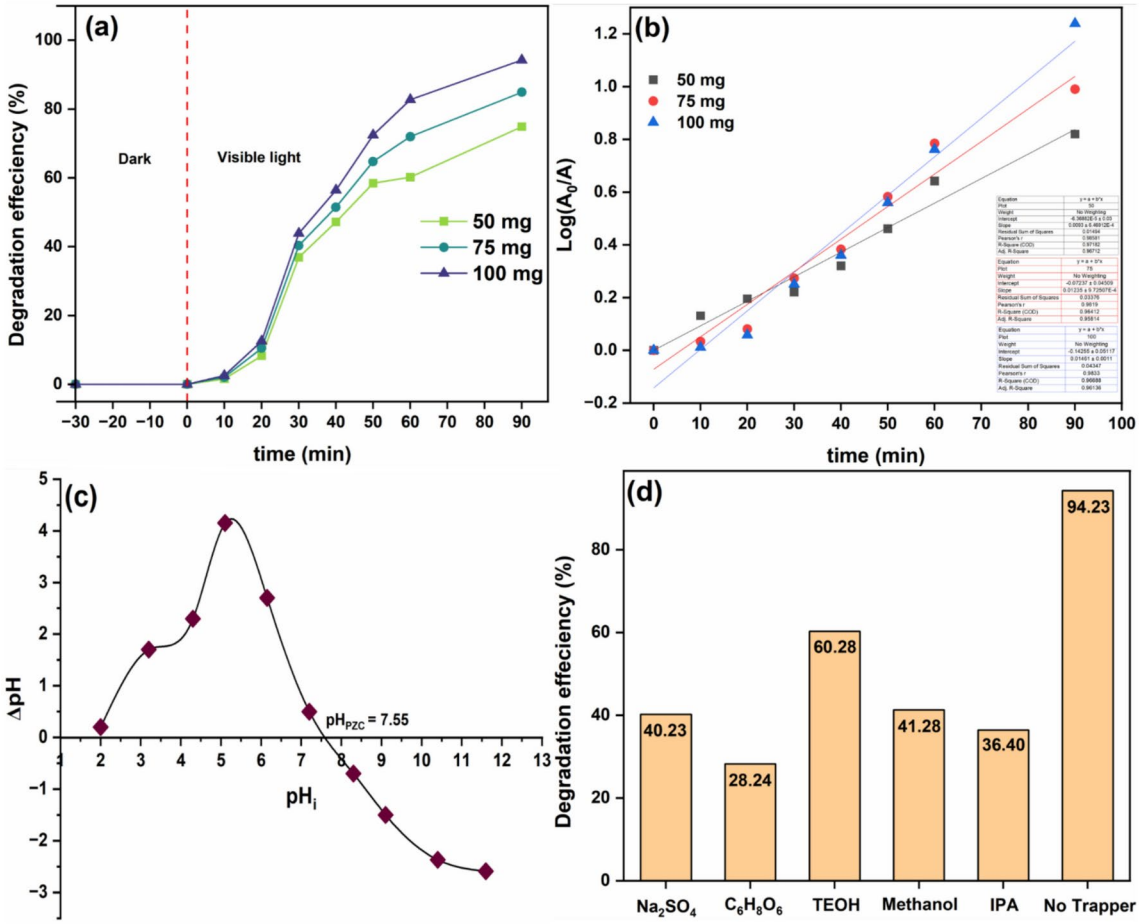

Fig. 12. Dosage-dependent TC-HCl removal percentage against irradiation time (**a**), 1st-order kinetics plot of TC-HCl degradation (**b**), trapping agent test (**c**), and pH_{PZC} evaluation (**d**).

Parameters	50 mg	75 mg	100 mg
k_1	0.0093	0.012	0.014
R^2	0.97	0.96	0.96

Table 5. Degradation kinetics parameters of TC-HCl antibiotic.

done by initially adjusting the reaction mixture to obtain specific values of pH (pH 3, 5, 7, 9, and 12) before initiating the process of photocatalysis under identical experimental conditions using dilute HCl and NaOH, respectively[65]. The efficiency of degradation was assessed by evaluating the absorbance of TC-HCl at its wavelength of interest using UV–Vis spectroscopy at equal intervals. Results depicted in Fig. 13a show that the maximum degradation efficiency of 94.26% was obtained at pH nearing 7. This confirms that neutral conditions facilitate the photocatalytic reaction. This study underlines the influence of pH on the surface charge of the photocatalyst, the ionization state of TC-HCl, and the generation of reactive species, which are all together affecting the degradation performance[66,67].

Evaluation of reusability was carried out through repeated TC-HCl degradation cycles conducted under identical conditions of experimentation (Fig. 13b). The photocatalyst recovered by the centrifugation after each cycle washed sufficiently with distilled water and allowed to dry could be reused again for the successive cycle. Photocatalytic degradation efficiency results are presented in up to five continuous cycles to see whether the activity and stability are sustained or reduced during these periods. The results have a gradual decay in efficiency and, at a point, exhibited 92.15% degradation in the 2nd cycle, 89.56% in the 3rd cycle, 70.27% in the 4th cycle, and 64.28% in the 5th cycle. These declines may result from the degradation of active sites or aggregation of catalysts and other structural degradations due to repeated use. These results showed that photocatalysts do possess some prospect in their potential use for real applications with little decline in activity following repeated runs[68].

Furthermore, the MF-10 sample centrifuged after the 1st-cycle of the degradation process was evaluated for morphology changes after interacting with TC-HCl. The results observed in Fig. 14a–c showcase no significant

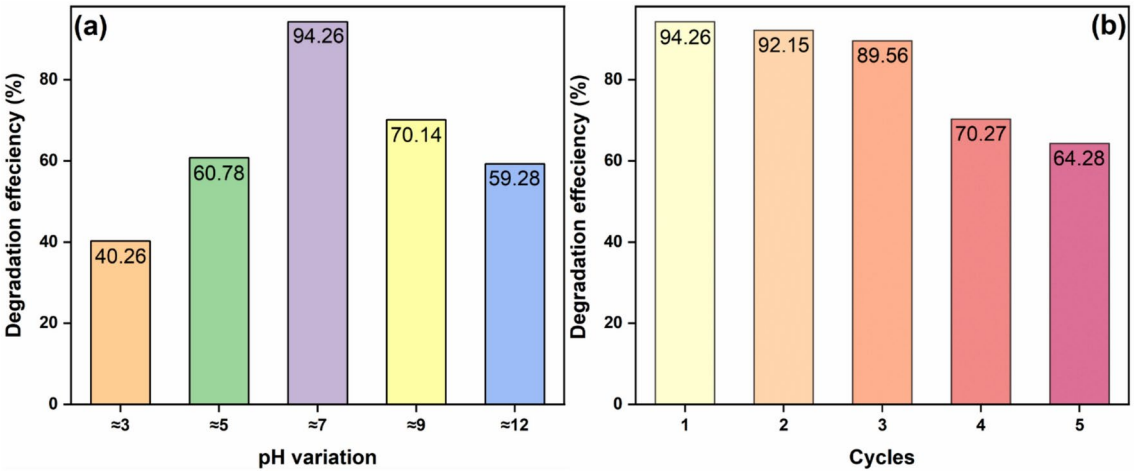

Fig. 13. pH effect on removal percentage (**a**) and reusability test of the recovered photocatalyst (**b**).

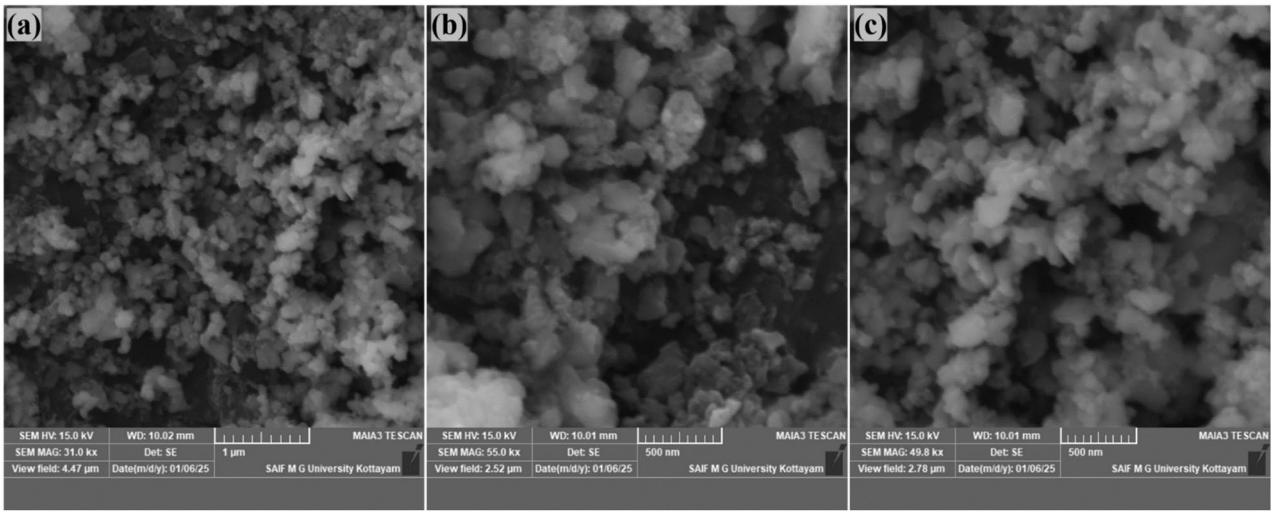

Fig. 14. FESEM images recorded after recovering the MF-10 sample from the degradation process of 1st-cycle.

S. no.	Photocatalyst	Antibiotics and degradation (%)	References
1.	Fe doped TiO_2–Bi_2O_3 nanocomposite	Cephalexin (74%)	[69]
2.	$CuAl_2O_4$–Cu–$Bi_4O_5Br_2$ Nanocomposite	Tetracycline (95.2%) Doxycycline (95.7%) Tetracycline + Doxycycline (95.4%)	[70]
3.	CeO_2: Au Nanoparticles	Tetracycline (86.4%) Ciprofloxacin (57.7%)	[71]
4.	Ag_2O nanoparticles	Ciprofloxacin (46%)	[72]
5.	$CuFe_2O_4$ nanoparticles	Tetracycline (95.8%)	[73]
6.	MnO_2: Fe^{3+} Nanoparticles	Tetracycline (94.26%)	This work

Table 6. Comparison of current MF-10 with various Photocatalyst.

change in the networked morphology except for the disappearance of the porous structure after interacting with the antibiotic TC-HCl. This is attributed to the improved stability of the sample even after cycle 1 of the degradation process. The results of the current catalyst are compared with the results of various catalysts against different antibiotics, which have been briefed in Table 6.

Possible degradation mechanism

The possible degradation mechanism (Fig. 15) of TC-HCl under photocatalytic conditions involves the generation of ROS where $\bullet O_2^-$ radical is considered the major species. Light absorption by the photocatalyst excites electrons from the valence band to the conduction band with energies higher or equal to the band gap, creating an electron–hole pair (e^-/h^+). The photogenerated electrons react with O_2 adsorbed on the catalyst's surface, forming $\bullet O_2^-$ radicals. Concurrently, holes (h^+) will oxidize water or hydroxyl ions (OH^-) and give hydroxyl radicals ($\bullet OH$)[74].

The $\bullet O_2^-$ radicals, being the main reactive species, initiate degradation of TC-HCl molecules through oxidative attack, degrading complex molecular structures into smaller intermediates. Further, degradation is enhanced by •OH and other species formed in the process that further oxidize the intermediates into simpler end products such as CO_2 and H_2O[75]. The mechanism is further supported by trapper experiments that revealed a strong diminution in the photocatalytic activity when particular scavengers were used, specifically those targeting $\bullet O_2^-$. The importance of superoxide radicals in facilitating the degradation process effectively is underscored. The suggested mechanism can be summarized through the following steps,

$$MF10 + h\nu \rightarrow e^- + h^+$$
$$e^- + O_2 \rightarrow \bullet O_2^-$$
$$h^+ + H_2O \rightarrow \bullet OH$$
$$TC - HCl + \bullet OH/\bullet O_2^- \rightarrow Degradedproduct \rightarrow CO_2 + H_2O$$

Adsorption of antibiotics on the surface of the photocatalyst might facilitates the degradation process by promoting their interaction with the reactive species. Here, drug adsorption onto the photocatalyst plays a prominent role in degrading TC-HCl. Adsorption improves the accessibility of the drug molecules for oxidative or photocatalytic degradation and thus enhances the efficiency of the process. Prolonged contact time further results in strong adsorption, with improved bond cleavage and mineralization of the antibiotic contaminants[76].

Completely degrading antibiotics does not imply that mineralization of TC-HCl has occurred, and CO_2 and H_2O have been formed; thus, in this study, the mineralization of TC-HCl by the MF-10 sample was studied by measuring TOC elimination. The results reveal a significant 73.36% mineralization of TC-HCl at 7.35 mg/L. This indicates that the complete mineralization of TC-HCl in the photocatalytic process will take more time than the photocatalytic elimination of TC-HCl. This occurrence might be due to the formation of various products that compete with TC molecules[77,78].

Stability assessment of photocatalyst

The pre-and post-degradation structural stability of the photocatalyst was assessed by recording the PXRD pattern and FTIR spectra of the initial and recovered MF-10 sample as depicted in Fig. 15. The PXRD results showcased in Fig. 16a reveal the stable cubic structure of MF-10 photocatalyst even after degrading the TC-HCl for 90 min. The same was observed in the FTIR results except for a small intensity drop at 1113.78 cm^{-1} (Fig. 16b) which was attributed to the absorption factor experienced by the catalyst. These findings suggest no change in chemical or structural aspects of the MF-10 photocatalyst even after recovering it after 90 min of degradation[79].

Conclusion

To conclude, the MnO_2: xFe^{3+} (MF-x, x = 0, 2, 4, 6, 8, and 10) nanoparticles were successfully prepared using the bio-reduction method with the help of leaf extract of *Tridax procumbens* as a capping agent. The optical band

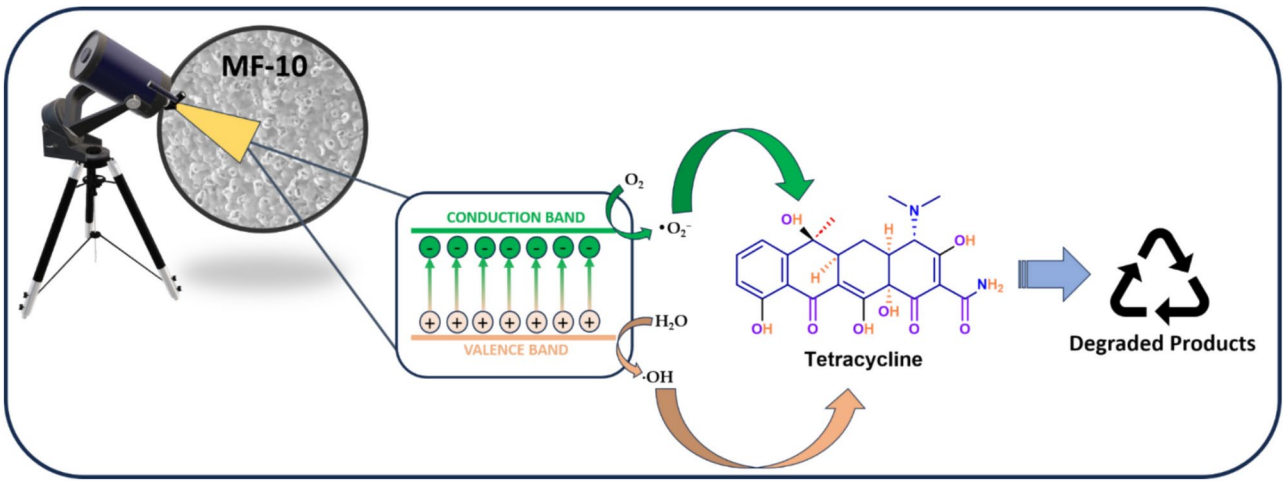

Fig. 15. Possible mechanism involved in the photocatalyst.

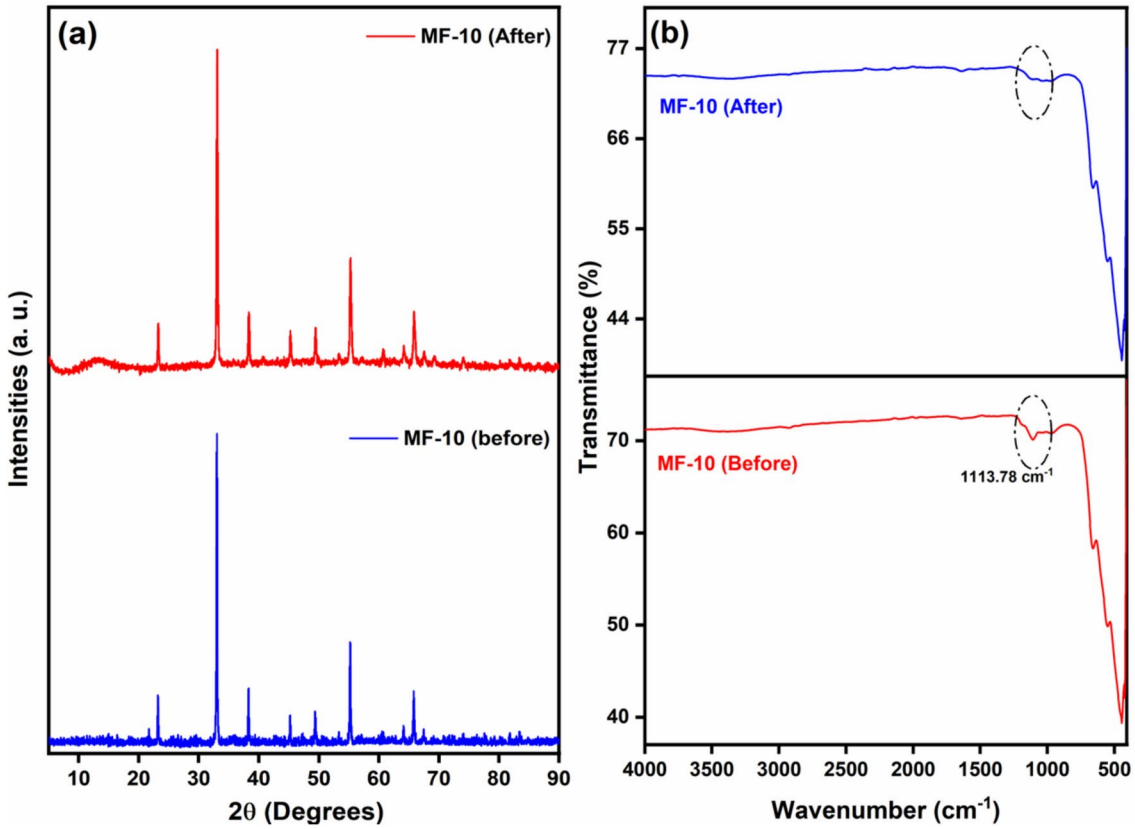

Fig. 16. PXRD (**a**) and FTIR (**b**) results of MF-10 photocatalyst before and after recycling.

gap of the as-synthesized MF-x catalysts has been calculated to be in the range of 2.06–0.97 eV, which proves the catalysts to be suitable for photocatalytic activity under visible light. The cubic crystalline structure identified by PXRD was also supported by Rietveld refinement with the crystallite size within the range of 39 to 74 nm. The FESEM and TEM results also showed that the surface of the synthesized catalysts had a porous structure, and the particle sizes were in accordance with the presence of PXRD, the results of elemental and components and XPS analysis properly confirmed Fe^{3+} ions doping into the MnO_2 lattice. Among the catalysts prepared, MF-10 demonstrated the highest photocatalytic activity, achieving 94.23% degradation of Tetracycline Hydrochloride (TC-HCl) within 90 min of visible light irradiation. The photocatalytic process followed first-order kinetics, and optimization of parameters such as pH and catalyst dosage highlighted the potential for wastewater treatment using these catalysts. Although degradation efficiency decreased after the fifth cycle, the catalysts maintained strong initial degradation efficiency under neutral pH conditions, indicating their promising potential for real-world applications. Also, a significant 73.36% mineralization of TC-HCl achieved was authenticated by TOC analysis. The structural stability of the photocatalyst after the degradation was assessed through PXRD and FTIR analysis, which reveal no changes after 90 min of TC-HCl degradation. In this study, bio-mediated MnO_2: Fe^{3+} nanoparticles were identified as an environmentally friendly and cost-effective solution to address environmental challenges. Future work should focus on improving the recyclability of these nanoparticles and scaling up the synthesis process to meet industrial demands for wastewater treatment. Further research into recyclability and large-scale applicability could enhance their effectiveness in environmental remediation.

Data availability

The datasets used and/or analysed during the current study available from the corresponding author on reasonable request.

Received: 3 February 2025; Accepted: 8 April 2025
Published online: 24 May 2025

References

1. Baaloudj, O. et al. Environmental fate, ecotoxicity, and remediation of heterocyclic pharmaceuticals as emerging contaminants: A review of long-term risks and impacts. *Organics* **6**, 1 (2025).
2. Natarajan, E. et al. *Sustainable Structural Materials: From Fundamentals to Manufacturing, Properties and Applications* (CRC Press, 2025).
3. Liu, Z. et al. Current status of emerging contaminant models and their applications concerning the aquatic environment: A review. *Water* **17**, 85 (2025).

4. Wang, C., et al. Photodegradation of typical psychotropic drugs in the aquatic environment: A critical review. *Environ. Sci. Process. Impacts* (2025).
5. Humelnicu, D. & Humelnicu, I. Significance of bioremediation approach: An overview for the wastewater treatment. In *Biotechnologies for Wastewater Treatment and Resource Recovery* (eds Srivastav, A. L. et al.) 297–309 (Elsevier, 2025).
6. Larcombe, E. et al. Current disease treatments for the ornamental pet fish trade and their associated problems. *Rev. Aquac.* **17**, e12948 (2025).
7. Verma, A. et al. Recent advancements in biochar and its composite for the remediation of hazardous pollutants. *Curr. Anal. Chem.* **21**, 15–56 (2025).
8. Nan, J. et al. Application of porous materials in photocatalytic treatment of wastewater. *Colloids Interfaces* **9**, 3 (2025).
9. Roostaee, M. & Ranjbar-Karimi, R. Emerging trends in carbon quantum dots: Synthesis, characterization, and environmental photodegradation applications. *Mater. Sci. Semicond. Process.* **188**, 109212 (2025).
10. Wang, X. et al. Photocatalytic degradation of organic pollutants and microplastics using Ag/TiO_2: Recent advances in mechanism, synthesis and properties. *Water Air Soil Pollut.* **236**, 30 (2024).
11. Vinayagam, R. et al. Synthesis of photocatalytic zinc oxide nanoflowers using *Peltophorum pterocarpum* pod extract and their characterization. *Appl. Nanosci.* **13**, 847–857 (2023).
12. Fan, L. et al. The antimicrobial activity and resistance evolution of nanomaterials: A review. *ACS Mater. Lett.* **7**, 1085–1111 (2025).
13. Ningthoukhongjam, P. et al. Multiphasic heterojunctions: A strategic approach to enhance the charge transfer dynamics of titania for superior solar photocatalytic hydrogen production. *Int. J. Hydrog. Energy* **113**, 133–146 (2025).
14. Vinayagam, R. et al. Green synthesized cobalt oxide nanoparticles with photocatalytic activity towards dye removal. *Environ. Res.* **216**, 114766 (2023).
15. Liang, Z. et al. Oxygen vacancies boost the efficacy of MnO_2 nanoparticles in catalyzing the hydrolytic degradation of organophosphate esters: implications for managing plastic additive pollution. *Environ. Sci. Nano* (2025).
16. ShekoftehNarm, T. et al. Plant-based synthesis of selenium-doped silver/magnesium oxide/zinc oxide nanocomposite using *Mentha pulegium* to investigate their photocatalytic and biological properties. *J. Mol. Struct.* **1320**, 139678 (2025).
17. Mohammad Hosseini, N. et al. Manganese ferrite-graphite oxide-chitosan nanocomposite for efficient dye removal from aqueous and textile wastewater under UV and sunlight irradiation. *Sci. Rep.* **15**, 866 (2025).
18. Karami, P. et al. Biosynthesized ZnO and MnO nanoparticles from Aegle marmelos peel extract for alkylphenol removal in wastewater. *Results Chem.* **13**, 102018 (2025).
19. Boyom-Tatchemo, F. W. et al. Plasma-synthesized combined nitrogen and cationic species doped-MnO_2: Impact on texture, optical properties, and photocatalytic activity. *Catal. Lett.* **155**, 8 (2024).
20. Anbarasu, K. & Devarajan, Y. Nanomaterials-based wastewater treatment: Addressing challenges and advancing sustainable solutions. *BioNanoScience* **15**, 149 (2024).
21. Akshita, K. S. et al. Photodeposition for highly effective photocatalytic materials. In *Emerging Trends in Photoredox Synthetic Transformation* (eds Sen, M. & Ray, D.) 403–449 (Springer, 2025).
22. Pan, Y. et al. Vanadium- and manganese-based metal-organic frameworks for potential environmental and catalysis applications. *Coord. Chem. Rev.* **522**, 216231 (2025).
23. Faramawy, A. M. et al. Tailoring the preparation, microstructure, FTIR, optical properties and photocatalysis of (Fe/Co) co-doped ZnO nanoparticles ($Zn_{0.9}FexCo_{0.1-x}O$). *Ceramics* **8**, 2 (2025).
24. Morais, D. F. S. et al. Sonochemical synthesis of $Ti_{1-x-y}Fe_xPb_yO_2$ (with x and y = 0, 0.01, 0.03, 0.07): Structural analysis, influence of radiation type on photocatalytic activity and assessment of antimicrobial properties. *Catal. Lett.* **155**, 6 (2024).
25. Majani, S. S. et al. Fe-doped $SrZrO_3$ nanostructures as photocatalyst: Solid-state synthesis and UV-light driven eradication of thymol blue dye. *Mater. Res. Bull.* **183**, 113184 (2025).
26. Irfan, M. F. et al. Structural, morphological, and electrocatalytic investigations of Fe_3O_4-doped Mn_3O_4 composite supported on carbonaceous materials derived from chitosan for oxygen reduction reaction. *New J. Chem.* **49**, 2308–2318 (2025).
27. Shen, Y. et al. Boosted photo-self-Fenton degradation activity by Fe-doped carbon dots as dual-function active sites for in-situ H_2O_2 generation and activation. *Sep. Purif. Technol.* **353**, 128529 (2025).
28. Rozina, et al. Valorization of waste seed oil from *Cupressus macrocarpa* L. for biodiesel production via green-synthesized iron oxide nanoparticles: A sustainable approach toward decarbonization. *Next Energy* **7**, 100218 (2025).
29. Redjili, S. et al. Green synthesis of silver oxide nanoparticles: Eco-friendly approach for sustainable solutions. *Ind. Crops Prod.* **223**, 120168 (2025).
30. Kadhem, A. A. & Alshamsi, H. A. Biosynthesis of Ag–ZnO/rGO nanocomposites mediated *Ceratophyllum demersum* L. leaf extract for photocatalytic degradation of Rhodamine B under visible light. *Biomass Convers. Biorefin.* **14**, 24655–24669 (2024).
31. Gbair, G. A. & Alshamsi, H. A. Facile green synthesis of CuO–ZnO nanocomposites from *Argyreia nervosa* leaves extract for photocatalytic degradation of Rhodamine B dye. *Biomass Convers. Biorefin.* **14**, 28117–28132 (2024).
32. Sumethra, R. et al. Ni blended NiO nanomaterial synthesis using three different plant extracts for effective dye wastewater remediation and biomedical application. *Mater. Sci. Eng. B* **313**, 117958 (2025).
33. Islam, A. et al. Recent advances on plant-based bioengineered nanoparticles using secondary metabolites and their potential in lung cancer management. *J. Future Foods* **5**, 1–20 (2025).
34. Mehra, V. et al. Green synthesis of gold nanoparticles (AuNPs) by using plant extract and their biological application: A review. *BioNanoScience* **15**, 18 (2024).
35. Seetharaman, J. et al. Evaluation of *Tridax procumbens* secondary metabolites anti-tuberculosis activity by in vitro and in silico methods. *Curr. Microbiol.* **82**, 50 (2024).
36. Singh, N. et al. Antibacterial potential and phytochemical analysis of two ethnomedicinally important plants. *Curr. Res. Microb. Sci.* **8**, 100297 (2025).
37. Ingole, V. V. et al. Phytochemistry and pharmacological aspects of *Tridax procumbens* (L.): A systematic and comprehensive review. *Phytomed. Plus* **2**, 100199 (2022).
38. Chinnappan, B. A. et al. *In vitro-in vivo* wound healing efficacy of *Tridax procumbens* extract loaded Carboxymethylcellulose film. *Int. J. Biol. Macromol.* **253**, 126695 (2023).
39. Akinola, A. O. & Adelowo, F. E. Chromatographic and spectrophotometric determination of some phenolic compounds in *Tridax procumbens* Linn Stem. *Chem. Afr.* **4**, 103–113 (2021).
40. Duke, J. A. *Handbook of Phytochemical Constituents of GRAS Herbs and Other Economic Plants* (CRC Press, 1992).
41. Arcelus, O. et al. FullProfAPP: A graphical user interface for the streamlined automation of powder diffraction data analysis. *J. Appl. Crystallogr.* **57**, 1676–1690 (2024).
42. Majani, S. S. et al. Nano-catalytic behavior of CeO_2 nanoparticles in dye adsorption: Synthesis through bio-combustion and assessment of UV-light-driven photo-adsorption of indigo carmine dye. *Heliyon* **10**, e35505 (2024).
43. Daphedar, A. B. et al. Evaluation of antioxidant and antibacterial activities of silver nanoparticles derived from *Limonia acidissima* L. fruit extract. *Curr. Res. Green Sustain. Chem.* **8**, 100399 (2024).
44. Varghese, D. et al. Synergistic design of CuO/$CoFe_2O_4$/MWCNTs ternary nanocomposite for enhanced photocatalytic degradation of tetracycline under visible light. *Sci. Rep.* **15**, 320 (2025).
45. Soldatova, A. V. et al. Biogenic and synthetic MnO_2 nanoparticles: Size and growth probed with absorption and Raman spectroscopies and dynamic light scattering. *Environ. Sci. Technol.* **53**, 4185–4197 (2019).

46. Vidhya, R. et al. A correlative effect of Fe^{3+} ion incorporation on the structure-optic and photocatalytic properties of CeO_2 nanoparticles. *J. Mater. Sci. Mater. Electron.* **35**, 1477 (2024).
47. Haque, B. M. et al. Influence of Fe^{2+}/Fe^{3+} ions in tuning the optical band gap of SnO_2 nanoparticles synthesized by TSP method: Surface morphology, structural and optical studies. *Mater. Sci. Semicond. Process.* **89**, 223–233 (2019).
48. Worku, A. K. et al. Enhancing oxygen reduction reaction activity of ε-MnO_2 nanoparticles via iron doping. *J. Phys. Chem. Solids* **157**, 110207 (2021).
49. Majani, S. S. et al. Dysprosium doped $SrCeO_3$ nanophosphors for advanced photochemical applications: Synthesis, characterization, photo-assisted dye degradation and latent fingerprint visualization. *Mater. Sci. Semicond. Process.* **182**, 108674 (2024).
50. Aarti, D. P. et al. Enhanced photocatalytic, photoluminescence and fingerprint properties of Dy^{3+} ions doped $BaZrO_3$ nanopowders for multifunctional applications. *Inorg. Chem. Commun.* **162**, 112255 (2024).
51. Zhang, X. et al. Fe-doped MnO_2 as an efficient catalyst for low temperature propane oxidation. *Mol. Catal.* **549**, 113468 (2023).
52. Majani, S. S. et al. Enhanced photocatalytic degradation activity of $SrCeO_3$ nanophosphors: Aloe vera gel-mediated synthesis and UV light-driven eradication of Titan Yellow dye. *Opt. Mater.* **162**, 116900 (2025).
53. Abrashev, M. V. et al. Raman spectra of R_2O_3 (R—rare earth) sesquioxides with C-type bixbyite crystal structure: A comparative study. *J. Appl. Phys.* https://doi.org/10.1063/1.4894775 (2014).
54. Zhang, L. et al. One-step hydrothermal synthesis of Fe^{3+}-doped sheet-like δ-MnO_2 for high-performance hybrid supercapacitors. *J. Energy Storage* **85**, 111136 (2024).
55. Mathews, N. R. et al. Fe doped TiO_2 powder synthesized by sol gel method: Structural and photocatalytic characterization. *J. Mater. Sci. Mater. Electron.* **26**, 5574–5584 (2015).
56. Vinayagam, R. et al. Emerging contaminant removal using eco-friendly zinc ferrite nanoparticles: Sunlight-driven degradation of tetracycline. *Emerg. Contam.* **11**, 100469 (2025).
57. Ashrafi-Saiedlou, S. et al. Biosynthesis and characterization of iron oxide nanoparticles fabricated using cell-free supernatant of Pseudomonas fluorescens for antibacterial, antifungal, antioxidant, and photocatalytic applications. *Sci. Rep.* **15**, 1018 (2025).
58. Mousa, S. A. et al. Enhanced photocatalytic activity of green synthesized zinc oxide nanoparticles using low-cost plant extracts. *Sci. Rep.* **14**, 16713 (2024).
59. Hayat, A. et al. Recent advances in ground-breaking conjugated microporous polymers-based materials, their synthesis, modification and potential applications. *Mater. Today* **64**, 180–208 (2023).
60. Mantilla, J. C. et al. Structural, morphological, and magnetic characterizations of $(Fe_{0.25}Mn_{0.75})_2O_3$ nanocrystals: A comprehensive stoichiometric determination. *Mater. Chem. Phys.* **328**, 129943 (2024).
61. Zheng, L. et al. Activation of peroxymonosulfate by magnetic $MnFe_2O_4$/MWCNT toward rhodamine B degradation: Efficiency, mechanism and influencing factors. *Water Air Soil Pollut.* **236**, 65 (2024).
62. Ahmed, S. et al. Enhanced adsorption and photocatalytic degradation of tetracycline antibiotics through novel I-Bi/Bi_2WO_6@MWCNTs heterostructure composite photocatalyst. *Environ. Res.* **268**, 120765 (2025).
63. Lu, H. et al. A novel $Bi_{12}O_{17}Cl_2$/GO/Co_3O_4 Z-type heterojunction photocatalyst with ZIF-67 derivative modified for highly efficient degradation of antibiotics under visible light. *J. Colloid Interface Sci.* **677**, 1052–1068 (2025).
64. Aziz, M. H. et al. $ZnFe_2O_4$/Cr_2O_3/MXene nanocomposite photocatalyst stimulates tetracycline antibiotic degradation under visible light irradiation: Toxicity evaluation and degradation mechanism. *Sep. Purif. Technol.* **354**, 128866 (2025).
65. Xu, M. et al. Construction of heterojunctions with in situ growth of ZnIn2S4 nanosheets on the surface of atomically dispersed Cu-modified MOFs for high-performance visible-light photocatalytic antibiotic degradation. *Sep. Purif. Technol.* **354**, 129093 (2025).
66. Al-Khayfawee, A. A. G. et al. Environmentally Friendly synthesis of zinc oxide nanoparticles using fructose as a carbohydrate agent: Investigation of photocatalytic degradation, antioxidant, and antibacterial activities. *BioNanoScience* **15**, 142 (2024).
67. Barkhor, H. et al. Construction of S-scheme $CuFe_{12}O_{19}$/CuS green nanocomposite for effective photocatalytic degradation of tetracycline from aqueous solution: Mechanism, recyclability, and kinetic study. *Appl. Water Sci.* **15**, 17 (2025).
68. Teng, J. et al. Honeycomb $BiFeO_3$ catalysts harvest mechanical energy from ultrasonic vibrations for efficient piezoelectric-catalyzed degradation of antibiotics. *Colloid Interface Sci. Commun.* **64**, 100813 (2025).
69. Abdeyazdan, Z. et al. Design, synthesis, and optimization of a novel ternary photocatalyst for degradation of cephalexin antibiotic in aqueous solutions. *Sci. Rep.* **15**, 8824 (2025).
70. Subhiksha, V. et al. Novel sandwich like interfacial engineering of Cu NPs on $CuAl_2O_4$ anchored $Bi_4O_5Br_2$ nanoflower Z-scheme nano-heterojunction for enhanced photocatalytic degradation of doxycycline and tetracycline. *J. Taiwan Inst. Chem. Eng.* **169**, 105952 (2025).
71. Huang, J. et al. Enhanced visible-light-driven photocatalytic degradation of tetracycline wastewater using surfactant-modified Au-loaded CeO_2 nanorods. *J. Environ. Manag.* **379**, 124893 (2025).
72. Tabassum, S. et al. Green synthesis of nano-Ag_2O using *Moringa oleifera* leaves for efficient photocatalytic and antimicrobial applications. *New J. Chem.* **49**, 1301–1313 (2025).
73. Dinesh, A. et al. Visible light photocatalytic degradation of tetracycline using copper ferrite nanoparticles synthesized via Glycine-Assisted combustion method. *Results Chem.* **13**, 102037 (2025).
74. Zhang, T. et al. Polymer-coated Fe_2O_3 nanoparticles for photocatalytic degradation of organic materials and antibiotics in water. *ACS Appl. Nano Mater.* **3**, 9200–9208 (2020).
75. Sharma, M. et al. Visible-light-driven photocatalytic degradation of tetracycline using heterostructured Cu_2O–TiO_2 nanotubes, kinetics, and toxicity evaluation of degraded products on cell lines. *ACS Omega* **7**, 33572–33586 (2022).
76. Li, X. et al. Strong adsorption of tetracycline on carbon blacks: An in-depth study of the adsorption mechanism. *J. Water Process Eng.* **70**, 106784 (2025).
77. Hasham Firooz, M. et al. Enhanced tetracycline degradation with TiO_2/natural pyrite S-scheme photocatalyst. *Sci. Rep.* **14**, 4954 (2024).
78. Ahmadi, M. et al. Enhanced photocatalytic degradation of tetracycline and real pharmaceutical wastewater using MWCNT/TiO_2 nano-composite. *J. Environ. Manag.* **186**, 55–63 (2017).
79. Hamza, A. M. & Alshamsi, H. A. Design of novel Z-scheme g-C_3N_4/TiO_2/$CuCo_2O_4$ heterojunctions for efficient visible light-driven photocatalyic degradation of rhodamine B. *Sci. Rep.* **14**, 23596 (2024).

Acknowledgements

The authors are thankful to the Director, Amrita Vishwa Vidyapeetham, Mysuru campus for providing the infrastructure facilities. The authors acknowledge the DST and the SAIF, Mahatma Gandhi University, Kottayam for characterization facilities. We acknowledge SCIF, SRMIST for providing the instrumentation facilities. The authors extend their appreciation to Researchers Supporting Project number (RSPD2025R734), King Saud University, Riyadh, Saudi Arabia. Mention of trade names or commercial products in this article is solely for the purpose of providing specific information and does not imply recommendation or endorsement by the USDA. USDA is an equal opportunity provider and employer.

Author contributions

S.S.M., V.M.A. and H.K.C.M.: Conceptualization, Methodology, Investigation, Formal analysis; S.S.M, P.S.S.S.: Data curation, Investigations, Formal analysis, Writing—Original draft preparation. M.I., C.S., C.A.C., K.E.H., P.R.B., R.G.A.: Visualization, Project administration, validation. S.P.K.: Resources, Supervision, Writing—Reviewing and Editing.

Declarations

Competing interests

The authors declare no competing interests.

Additional information

Supplementary Information The online version contains supplementary material available at https://doi.org/10.1038/s41598-025-97862-y.

Correspondence and requests for materials should be addressed to M.A.V., R.G.A. or S.P.K.

Reprints and permissions information is available at www.nature.com/reprints.

Publisher's note Springer Nature remains neutral with regard to jurisdictional claims in published maps and institutional affiliations.